A Spectral Survey of CH₃CCH in the Hot Molecular Core G331.512-0.103

Julia C. Santos[1,2] ⬩, Leonardo Bronfman[3] ⬩, Edgar Mendoza[1,4] ⬩, Jacques R. D. Lépine[1] ⬩, Nicolas U. Duronea[5,6],
Manuel Merello[3] ⬩, and Ricardo Finger[3]

[1] Instituto de Astronomia, Geofísica e Ciências Atmosféricas; Universidade de São Paulo, Rua do Matão, 1226, São Paulo, SP, Brazil
[2] Laboratory for Astrophysics, Leiden Observatory, Leiden University, P.O. Box 9513, 2300 RA Leiden, The Netherlands; santos@strw.leidenuniv.nl
[3] Departamento de Astronomía; Universidad de Chile, Casilla 36-D, Santiago de Chile, Chile
[4] Observatório do Valongo; Universidade Federal do Rio de Janeiro, Ladeira do Pedro Antônio, 43, Rio de Janeiro, RJ, Brazil
[5] Instituto de Astrofísica de La Plata (UNLP-CONICET), La Plata, Argentina
[6] Facultad de Ciencias Astronómicas y Geofísicas, Universidad Nacional de La Plata, Paseo del Bosque s/n, 1900, La Plata, Argentina
Received 2021 August 28; revised 2021 November 2; accepted 2021 November 3; published 2022 January 20

Abstract

A spectral survey of methyl acetylene (CH₃CCH) was conducted toward the hot molecular core/outflow G331.512-0.103. Our APEX observations allowed the detection of 41 uncontaminated rotational lines of CH₃CCH in the frequency range between 172 and 356 GHz. Through an analysis under the local thermodynamic equilibrium assumption, by means of rotational diagrams, we determined $T_{exc} = 50 \pm 1$ K, $N(CH_3CCH) = (7.5 \pm 0.4) \times 10^{15}$ cm², $X[CH_3CCH/H_2] \approx (0.8\text{–}2.8) \times 10^{-8}$, and $X[CH_3CCH/CH_3OH] \approx 0.42 \pm 0.05$ for an extended emitting region ($\sim 10''$). The relative intensities of the $K = 2$ and $K = 3$ lines within a given K-ladder are strongly negatively correlated to the transitions' upper J quantum number ($r = -0.84$). Pure rotational spectra of CH₃CCH were simulated at different temperatures, in order to interpret this observation. The results indicate that the emission is characterized by a nonnegligible temperature gradient with upper and lower limits of ~ 45 and ~ 60 K, respectively. Moreover, the line widths and peak velocities show an overall strong correlation with their rest frequencies, suggesting that the warmer gas is also associated with stronger turbulence effects. The $K = 0$ transitions present a slightly different kinematic signature than the remaining lines, indicating that they might be tracing a different gas component. We speculate that this component is characterized by lower temperatures and therefore larger sizes. Moreover, we predict and discuss the temporal evolution of the CH₃CCH abundance using a two-stage zero-dimensional model of the source constructed with the three-phase Nautilus gas-grain code.

1. Introduction

Star-forming regions play a key role in building the complex inventory of chemical species detected in astronomical environments, which in turn serve as powerful tools to study their surroundings. Through the observation of molecular emission lines, it is possible to constrain both the physical conditions and the chemical evolution of circumstellar sources, shedding light on the formation processes that connect different evolutionary stages of star formation. Methyl acetylene (CH₃CCH), also known as propyne, is a particularly good temperature probe and has therefore been widely explored toward various star-forming objects (e.g., Fontani et al. 2002; Bisschop et al. 2007; Fayolle et al. 2015; Giannetti et al. 2017; Andron et al. 2018; Calcutt et al. 2019).

Massive stars ($L > 10^3\,L_\odot$; $M > 8\,M_\odot$) greatly affect their surroundings through their feedback and the production of heavy elements. The formation process of those stars, however, is still less well understood in comparison to the low-mass counterparts. Observational disadvantages, such as their complex cluster environments ($n_\star \gtrsim 100$ pc^{-3}) and large distances involved ($d \geqslant 1$ kpc), together with a considerably shorter evolutionary timescale ($t_{KH} \leqslant 10^4$ yr for O-type stars), substantially impair the development of a solid massive-star formation paradigm (Garay

& Lizano 1999; Zinnecker & Yorke 2007; Tan et al. 2014; Krumholz 2015, pp 43–80; Silva et al. 2017; Rosen et al. 2020).

Despite the lack of a thoroughly defined evolutionary sequence, some precursors of high-mass stars are well established. One example are hot molecular cores (HMCs), which are one of the first manifestations of massive-star formation (Cesaroni 2005). They are characterized by relatively high temperatures (>100 K) and high densities ($n_{H_2} \sim 10^5\text{–}10^8$ cm^{-3}), linked with a compact (<0.1 pc), luminous ($>10^4\,L_\odot$), and massive ($\sim 10\text{–}1000\,M_\odot$) molecular core (Heaton et al. 1989; Gomez et al. 1995; Cesaroni et al. 1998; Cesaroni 2005; Bonfand et al. 2019). HMCs are associated with a rich molecular emission spectrum, which carries information on their chemical and physical properties, as well as their morphology and evolutionary stage (e.g., Caselli et al. 1993; Comito et al. 2005; Herbst & van Dishoeck 2009; Allen et al. 2018; Bonfand et al. 2019; Jørgensen et al. 2020; Gieser et al. 2021).

1.1. The Source: G331.512-0.103

G331.512-0.103 (henceforth G331) is a massive and energetic HMC/outflow system. It is located within the millimeter source G331.5-0.1 (see Merello et al. 2013b and references therein), at the tangent point of the Norma spiral arm (~ 7.5 kpc; Bronfman et al. 1985, 2008), and which consists of a singularly extended and luminous complex at the center of a giant molecular cloud (GMC). The parent GMC is located at the peak region of the southern molecular and massive-star

formation rings (i.e., the peaks of the azimuthally averaged radial distributions of molecular gas and of regions of massive-star formation; Bronfman et al. 2000). Likewise, it is one of the most massive and active star-forming clouds in the southern Galaxy (García et al. 2014). Observational evidence indicates that a young massive stellar object (YMSO) at the center of G331 drives a powerful outflow with $\sim 55\,M_\odot$ of mass and a momentum of $\sim 2.4 \times 10^3\,M_\odot$ km s^{-1} (Bronfman et al. 2008), with lobes closely aligned with the line of sight. Observations with the Atacama Large Millimeter/submillimeter Array (ALMA) of the SiO $(8-7)$, H^{13}CO$^+$ $(4-3)$, HCO$^+$ $(4-3)$, and CO $(3-2)$ transitions revealed an expanding bubble geometry driven by stellar winds, which probably arises from the protostar confined in a compact H II region of $\sim 5''$ (projected size of ~ 0.2 pc; Merello et al. 2013a). Its emission spectrum exhibits great chemical lavishness, from common radicals and carbon-chain molecules to prebiotic and complex organic species (Merello et al. 2013a, 2013b; Mendoza et al. 2018; Duronea et al. 2019; Hervías-Caimapo et al. 2019; Canelo et al. 2021). All those factors make G331 an exquisite source for astrochemical investigations by means of spectral surveys in submillimeter wavelengths.

1.2. The Molecule: Methyl Acetylene

More than 200 molecules have been hitherto detected toward the interstellar and circumstellar media (e.g., McGuire 2018). Methyl acetylene (CH$_3$CCH) has been detected in a wide variety of sources. It has been proven to be a reliable tracer of physical conditions, such as temperature and density, and has been extensively studied toward star-forming regions (e.g., Buhl & Snyder 1973; Lovas et al. 1976; Hollis et al. 1981; Kuiper et al. 1984; Guzmán et al. 2018; Taniguchi et al. 2018; Bøgelund et al. 2019; Calcutt et al. 2019). It has also been observed toward extragalactic sources, such as M82, NGC 253, and NGC 1068 (Mauersberger et al. 1991; Qiu et al. 2020), and toward a planetary nebula (Schmidt & Ziurys 2019).

The rotational transitions of CH$_3$CCH are characterized by two quantum numbers, namely, the total angular momentum (J) and its projection on the principal symmetry axis (K) (Townes & Schawlow 1975; Müller et al. 2000). Because it is a symmetric rotor, CH$_3$CCH presents many transitions that are closely spaced in frequency: the so-called K-ladders. The capability to observe many lines in the same bandwidth reduces calibration uncertainties and yields more precise predictions. Moreover, due to its small electric dipole moment ($\mu = 0.75$ D; Dubrulle et al. 1978), line thermalization occurs at densities as low as $\sim 10^4$ cm^{-3} (e.g., Bergin et al. 1994; Fontani et al. 2002; Molinari et al. 2016). Transitions with $\Delta K \neq 0$ are forbidden, and therefore the relative populations of different K-ladders are dictated by collisions. As a result, CH$_3$CCH acts as an excellent temperature probe. Indeed, this molecule's temperature sensitivity makes it a reliable tracer of physical conditions and passive heating (Molinari et al. 2016; Giannetti et al. 2017).

Aside from observational advantages, the intrinsic spectroscopic properties of CH$_3$CCH can directly affect the observed spectra and therefore can give powerful insights on the physics of the emitting gas. Rotational spectroscopy is a conspicuously fruitful technique to infer information on the molecular species and its environment (e.g., Domenicano & Hargittai 1992; Winnewisser et al. 2003; Grubbs & Cooke 2010) and is nowadays highly assisted by quantum chemistry (e.g., Puzzarini et al. 2012a, 2012b; Cernicharo et al. 2015; Cazzoli et al. 2016;

McGuire et al. 2016; Cerqueira et al. 2020; Santos et al. 2020). The rotational Hamiltonian is described in terms of the zeroth-order rotational constants (A, B, and C) and the higher-order centrifugal distortion constants (e.g., D_J, D_{JK}, D_K, H_J, H_{JK}, H_{KJ}, and H_K, for symmetric tops). These constants can be measured from laboratory experiments guided by theoretical simulations, which in turn play a fundamental role in line assignments of radioastronomical observations (e.g., Belloche et al. 2014, 2019; Coutens et al. 2016; Melli et al. 2018).

In this work, we conducted a spectral survey of CH$_3$CCH toward G331, resulting in the detection of 41 uncontaminated lines. The goal of this work is to analyze the excitation conditions of methyl acetylene in this source, which gives information on the chemical and physical conditions of the gas and consequently helps in unveiling the early stages of massive-star formation. Quantum-chemical properties associated with this molecule are especially relevant to explore the small-scale structure of the source. In Section 2, we delineate the observational procedure. In Section 3, we present our results on the line identifications and radiative analysis. Those results are then discussed in Section 4. The observed abundance is discussed in the context of a chemical model of our source in Section 5. Finally, our conclusions and perspectives are presented in Section 6.

2. Observations

The observations were obtained with the Atacama Pathfinder EXperiment (APEX) telescope (Güsten et al. 2006) using the single-point mode toward the coordinates of the source (Bronfman et al. 2008) R.A., decl. (J2000) = $16^h12^m10^s.1$, $-51°28'38''.1$. The Swedish-ESO PI Instrument (SEPIA180; Belitsky et al. 2018) was used, together with APEX-1 and APEX-2 receivers of the Swedish Heterodyne Facility Instrument (SHeFI; Vassilev et al. 2008), to observe nine frequency setups within the intervals 170–205 GHz and 222–307 GHz, respectively. As a back end for the APEX-1 and APEX-2 receivers, the eXtended bandwidth Fast Fourier Transform Spectrometer2 (XFFTS2) was used, which consists of two units with 2.5 GHz bandwidth divided into 32,768 channels each. SEPIA180 is a dual-polarization sideband-separated (2SB) receiver, which is able to observe two 4 GHz bands, separated by 12 GHz, simultaneously. Thus, it covers 100% of the SEPIA ALMA Band 5 receiver channel IF band (159–211 GHz). The spectral resolution, corresponding to velocity resolutions, was obtained between 0.06 and 0.13 km s^{-1} for a noise level of ~ 30–50 mK. While all analyses were performed with the original data, for further clarity and uniformity in their graphical depiction, the resolution of the spectra exhibited in the present work was degraded to a common value of 1 km s^{-1}. The original intensity, obtained in a scale of antenna temperature corrected for atmospheric attenuation (T_A), was converted to the main-beam temperature (T_{mb}) scale using the main-beam efficiencies $\eta_{mb} = 0.80$ for SEPIA180,[7] and $\eta_{mb} = 0.75$ and 0.73 for APEX-1 and APEX-2, respectively[8] (e.g., Canelo et al. 2021). The half-power beamwidth (HPBW) values vary between $\sim 17''$ and $39''.9$ We adopted a calibration uncertainty of about 10% (Dumke & Mac-Auliffe 2010).
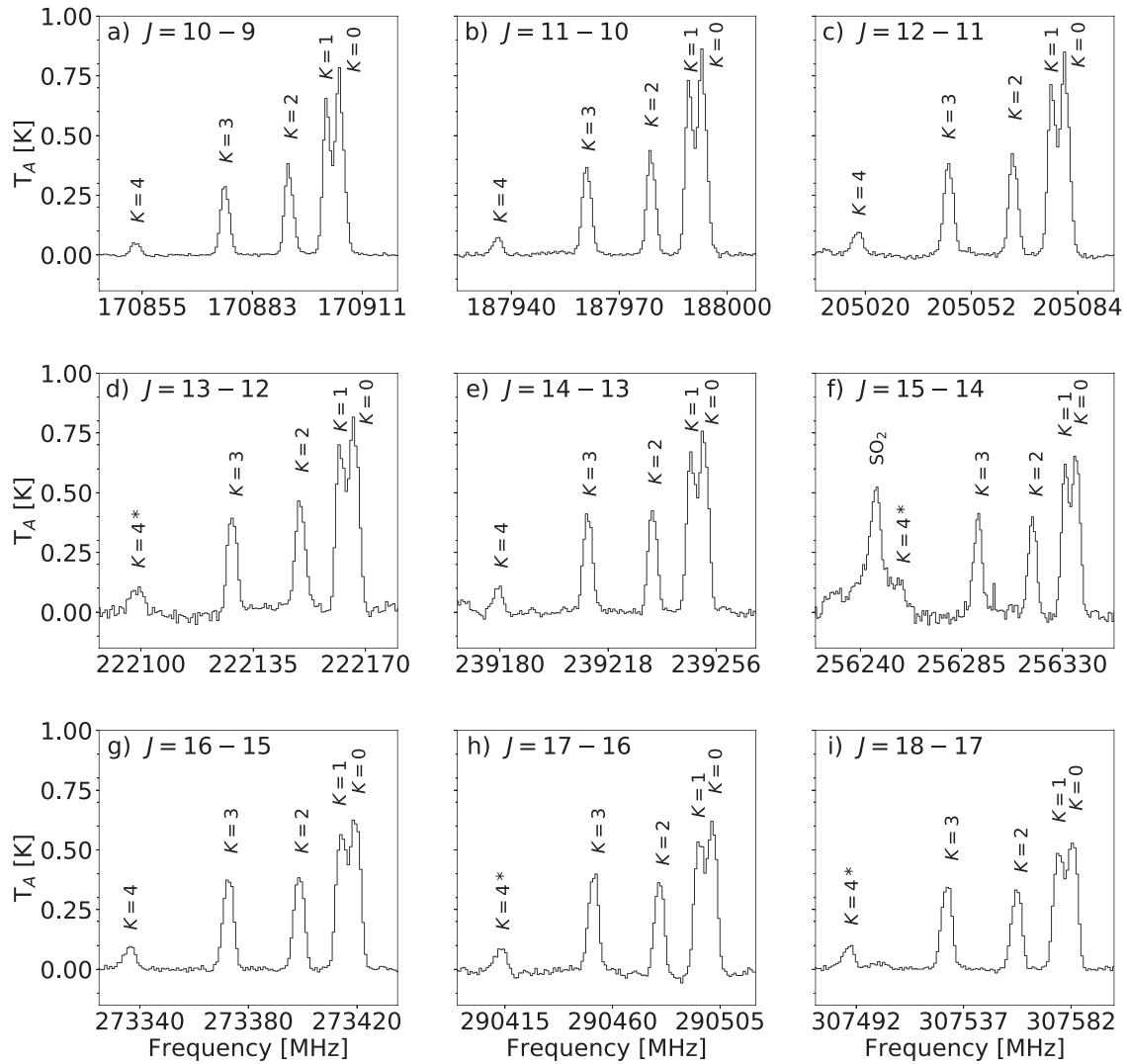
The data reduction was carried out using the CLASS package of the GILDAS software[10] (Pety et al. 2005;

Figure 1. Spectral lines of CH_3CCH identified toward G331 across the frequency range of 170.850–307.590 GHz. Each panel displays the K-ladder lines for the rotational transitions (a) $J = 10_K - 9_K$, (b) $J = 11_K - 10_K$, (c) $J = 12_K - 11_K$, (d) $J = 13_K - 12_K$, (e) $J = 14_K - 13_K$, (f) $J = 15_K - 14_K$, (g) $J = 16_K - 15_K$, (h) $J = 17_K - 16_K$, and (i) $J = 18_K - 17_K$. The asterisk indicates lines below the 3σ threshold. Linear baselines were subtracted from each spectrum, and the spectral resolution was resampled to a common channel of approximately 1 km s^{-1}.

Gildas Team [2013]). First-degree polynomial baselines were removed from each individual scan, which were subsequently averaged into a final spectrum. Line identifications were performed using the Weeds extension of CLASS, in combination with spectroscopic databases such as NIST[11] Recommended Rest Frequencies for Observed Interstellar Molecular Microwave Transitions (Lovas [2004]), CDMS[12] (Müller et al. [2001], [2005]; Endres et al. [2016]), JPL[13] (Pickett et al. [1998]), and Splatalogue.[14] The establishment of a molecular identification warrants the satisfaction of a set of standard requirements (Snyder et al. [2005]). Accordingly, the following criteria were used in order to confirm a detection: the peak frequencies of the observed lines should be consistent with the systemic velocity of G331 ($V_{lsr} \sim -90$ km s^{-1}), the intensities of the observed lines should surpass the threshold of 3 rms noise, and lines predicted through local thermodynamic equilibrium (LTE) modeling should agree with

the observations. The radiative studies, including the optical depth estimation, were based on analyses carried out with the CASSIS software[15] (Vastel et al. [2015])—assuming LTE. CASSIS has been developed by IRAP-UPS/CNRS.

3. Results

3.1. Line Analysis of CH₃CCH

We detected a total of 41 lines of CH_3CCH spread across the spectral band, from $\sim$170.84 to $\sim$307.60 GHz. Considering that CH_3CCH exhibits a K-ladder spectral signature, in Figure 1 we have displayed all the observed K-ladder structures from the $J = 10-9$ to $J = 18-17$ rotational levels.

Spectroscopic parameters obtained through Gaussian fittings to the lines are summarized in Table 1. The fittings were performed to the spectra at their full resolution of $\sim$0.06–0.13 km s^{-1}.

For each observed J_u level, all transitions with $K = 3-0$ were detected. In some cases (see Table 1), lines with $K = 4$ were not detectable above the 3 rms noise threshold and were

Table 1
Spectral Lines of CH$_3$CCH Observed toward G331 and Their Parameters Obtained from Gaussian Fits

| Quantum Numbers				Frequency (MHz)	E_u (K)	A_u (10^{-5} s^{-1})	$\int T_A dv$ (K km s^{-1})	V_{lsr} (km s^{-1})	FWHM (km s^{-1})
J_u	K_u	J_l	K_l						
10	4	9	4	170,853.576	160.7	1.43	0.24 ± 0.01	−90.02 ± 0.09	4.4 ± 0.2
10	3	9	3	170,876.410	110.1	1.55	1.43 ± 0.01	−89.89 ± 0.02	4.57 ± 0.06
10	2	9	2	170,892.726	74.0	1.63	1.75 ± 0.02	−89.77 ± 0.03	4.41 ± 0.06
10	1	9	1	170,902.518	52.3	1.68	3.04 ± 0.06	−89.74 ± 0.04	4.4 ± 0.1
10	0	9	0	170,905.783	45.1	1.70	3.95 ± 0.04	−89.34 ± 0.02	4.99 ± 0.06
11	4	10	4	187,936.230	169.7	1.97	0.38 ± 0.01	−90.40 ± 0.08	4.76 ± 0.2
11	3	10	3	187,961.342	119.2	2.10	1.87 ± 0.02	−89.96 ± 0.02	4.68 ± 0.05
11	2	10	2	187,979.286	83.0	2.20	2.07 ± 0.02	−89.84 ± 0.02	4.45 ± 0.06
11	1	10	1	187,990.055	61.4	2.25	3.53 ± 0.07	−89.83 ± 0.04	4.6 ± 0.1
11	0	10	0	187,993.645	54.1	2.27	4.43 ± 0.04	−89.39 ± 0.02	5.06 ± 0.06
12	4	11	4	205,018.114	179.6	2.63	0.48 ± 0.01	−89.89 ± 0.07	5.0 ± 0.2
12	3	11	3	205,045.501	129.0	2.77	1.97 ± 0.02	−89.99 ± 0.02	4.80 ± 0.06
12	2	11	2	205,065.070	92.9	2.88	2.04 ± 0.02	−89.86 ± 0.02	4.52 ± 0.05
12	1	11	1	205,076.816	71.2	2.94	3.51 ± 0.06	−89.94 ± 0.04	4.6 ± 0.1
12	0	11	0	205,080.732	64.0	2.96	4.46 ± 0.05	−89.43 ± 0.03	5.18 ± 0.07
13	4	12	4	222,099.153[a]	190.2	3.42	0.72 ± 0.04	−89.9 ± 0.2	6.6 ± 0.4
13	3	12	3	222,128.815	139.7	3.57	1.97 ± 0.04	−90.04 ± 0.04	4.5 ± 0.1
13	2	12	2	222,150.010	103.5	3.69	2.33 ± 0.03	−90.07 ± 0.03	4.84 ± 0.08
13	1	12	1	222,162.730	81.9	3.75	3.74 ± 0.09	−90.15 ± 0.06	5.0 ± 0.1
13	0	12	0	222,166.971	74.6	3.78	4.43 ± 0.06	−89.52 ± 0.03	5.24 ± 0.09
14	4	13	4	239,179.281	201.7	4.34	0.44 ± 0.02	−90.62 ± 0.07	4.1 ± 0.2
14	3	13	3	239,211.215	151.1	4.51	2.02 ± 0.03	−90.15 ± 0.03	4.55 ± 0.07
14	2	13	2	239,234.034	115.0	4.63	2.08 ± 0.03	−90.09 ± 0.03	4.51 ± 0.06
14	1	13	1	239,247.728	93.3	4.70	3.69 ± 0.07	−90.29 ± 0.05	5.2 ± 0.1
14	0	13	0	239,252.294	86.1	4.73	4.25 ± 0.06	−89.50 ± 0.03	5.34 ± 0.09
15	4	14	4	256,258.426[a]	214.0	5.41	1.2 ± 0.1	−89.1 ± 0.3	7.3 ± 0.7
15	3	14	3	256,292.630	163.4	5.59	2.29 ± 0.06	−90.14 ± 0.06	5.1 ± 0.1
15	2	14	2	256,317.071	127.3	5.72	2.13 ± 0.06	−90.02 ± 0.06	4.9 ± 0.1
15	1	14	1	256,331.739	105.7	5.80	3.23 ± 0.06	−90.14 ± 0.04	4.8 ± 0.1
15	0	14	0	256,336.629	98.4	5.83	4.00 ± 0.05	−89.54 ± 0.04	5.43 ± 0.09
16	4	15	4	273,336.519	227.1	6.64	0.58 ± 0.02	−90.30 ± 0.08	5.4 ± 0.2
16	3	15	3	273,372.990	176.6	6.84	2.08 ± 0.02	−90.17 ± 0.03	4.91 ± 0.07
16	2	15	2	273,399.051	140.4	6.97	2.13 ± 0.02	−90.16 ± 0.03	4.93 ± 0.07
16	1	15	1	273,414.692	118.8	7.06	3.48 ± 0.06	−90.42 ± 0.04	5.5 ± 0.1
16	0	15	0	273,419.906	111.5	7.09	3.82 ± 0.02	−89.66 ± 0.02	5.48 ± 0.09
17	4	16	4	290,413.488[a]	241.0	8.04	0.58 ± 0.02	−90.2 ± 0.1	5.3 ± 0.2
17	3	16	3	290,452.224	190.5	8.25	2.40 ± 0.05	−90.47 ± 0.04	5.4 ± 0.1
17	2	16	2	290,479.904	154.4	8.40	2.07 ± 0.03	−90.27 ± 0.03	4.9 ± 0.1
17	1	16	1	290,496.516	132.7	8.49	3.53 ± 0.06	−90.68 ± 0.04	5.7 ± 0.1
17	0	16	0	290,502.054	125.5	8.52	3.81 ± 0.05	−89.88 ± 0.04	5.4 ± 0.1
18	4	17	4	307,489.264[a]	255.8	9.62	0.52 ± 0.01	−90.13 ± 0.07	5.2 ± 0.2
18	3	17	3	307,530.263	205.3	9.84	1.88 ± 0.02	−90.23 ± 0.03	4.90 ± 0.06
18	2	17	2	307,559.559	169.1	10.00	1.73 ± 0.02	−90.23 ± 0.03	4.76 ± 0.07
18	1	17	1	307,577.141	147.5	10.10	2.91 ± 0.04	−90.50 ± 0.03	5.39 ± 0.08
18	0	17	0	307,583.003	140.3	10.10	3.27 ± 0.05	−89.76 ± 0.04	5.6 ± 0.1

Note.
[a] Lines below the 3σ threshold.

not considered in our analyses. Nevertheless, all K-ladders include a minimum of four detected transitions. The CH$_3$CCH lines present a low velocity dispersion (± 0.68 km s^{-1}) around the systemic velocity of the source and a mean systemic velocity of $\bar{V}_{lsr} = -90.0 \pm 0.3$ km s^{-1}, obtained through averaging the velocities of all 41 lines. Line profiles are narrow, with average values of 4.9 ± 0.8 km s^{-1}, and observed line widths also show

an overall small dispersion, with FWHM values ranging from 4.15 to 5.68 km s^{-1}. This indicates that the emission originates from a quiescent region, as will be discussed in Section 4.1.

3.2. Rotational Diagrams and Physical Properties

In order to estimate the excitation temperature (T_{exc}) and column density (N) of CH$_3$CCH, rotational diagrams were
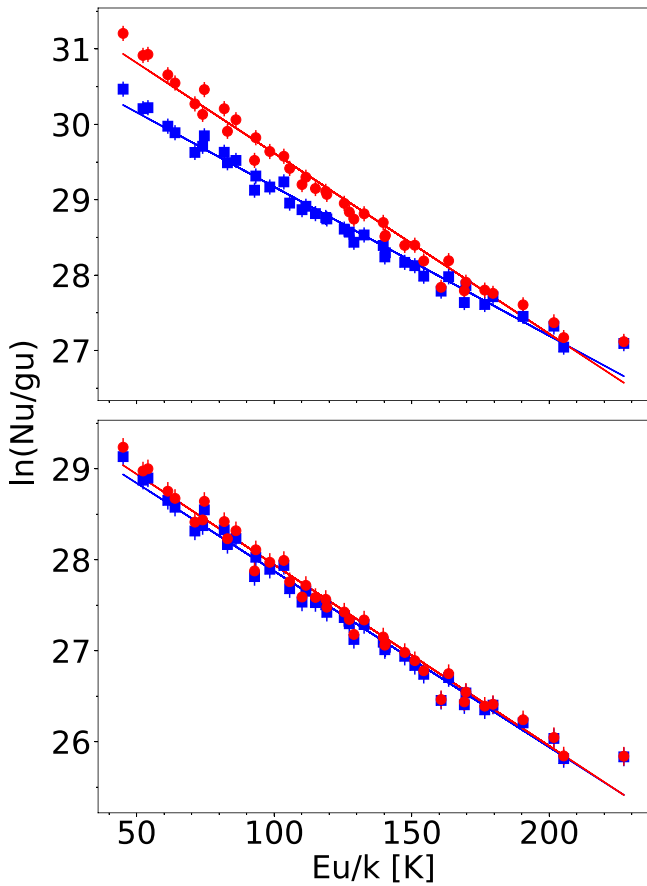
Figure 2. Top panel: rotational diagram of the CH$_3$CCH lines for a source size of 5″. Red circles and blue squares correspond to the lines with and without opacity corrections, respectively. Least-squares fits to the points are also shown in their respective color. The error bars are propagated from the Gaussian fit to the lines and take into consideration a calibration uncertainty of 10% (Santos 2021). Bottom panel: same as the top panel, but for a source size of 10″ in diameter.

constructed. Under the assumption of LTE, one can derive the T_{exc} and N of an optically thin emission that uniformly fills the antenna beam from

$$\ln\left(\frac{N_u}{g_u}\right) = \ln\left(\frac{N}{Q(T_{exc})}\right) - \frac{E_u}{k_B T_{exc}}, \qquad (1)$$

where Q is the species' partition function at T_{exc} and k_B is the Boltzmann constant. N_u, g_u, and E_u are, respectively, the column density, the statistical weight, and the energy of the upper level (Goldsmith & Langer 1999). A plot of $\ln(N_u/g_u)$ versus E_u of the observed lines will thus correspond to a straight line, whose slope and y-intercept are defined by $1/T_{exc}$ and $\ln(N/Q(T_{exc}))$, respectively. For a spatially unresolved emitter, a beam dilution correction factor, $(\Delta\Omega_a/\Delta\Omega_s)$, should be introduced on the right-hand side of Equation (1). For a preliminary analysis, we adopted an average source size of 5″, in accordance with previous observations of G331 (e.g., Hervías-Caimapo et al. 2019; Canelo et al. 2021, and references therein).

The rotational diagram of CH$_3$CCH constructed under the assumption of optically thin lines is displayed in blue in the top panel of Figure 2. We derived $N(CH_3CCH) = (2.5 \pm 0.1) \times 10^{16}$ cm^{-2} and $T_{exc} = 51 \pm 1$ K from the fit ($\chi^2_{red} = 1.49$). The

uncertainties were computed following the formalism of the CASSIS software,[16] which takes into account the calibration error of 10%.

To explore the validity of the optically thin assumption, we estimated the lines' optical depths (τ) using CASSIS. The opacity correction is incorporated into Equation (1) through iterative calculations of the optical depth correction factor C_τ (Goldsmith & Langer 1999), associated with the photon escape probability:

$$C_\tau = \frac{\tau}{1 - e^{-\tau}}. \qquad (2)$$

The optical depth correction factor is introduced on the right-hand side of Equation (1). The iterations stop when a solution for T_{exc} and N converges, that is to say, when the difference between the last two iterations is smaller than 1%. The opacity-corrected rotational diagram of CH$_3$CCH is displayed in red in both panels of Figure 2. From the fit ($\chi^2_{red} = 2.57$) we obtained $N(CH_3CCH) = (4.5 \pm 0.3) \times 10^{16}$ cm^{-2} and $T_{exc} = 42 \pm 1$ K. This correction leads to a new scaling of the diagram's ordinate axis, resulting in a decrease of 17% and an increase of 80% in the values of T_{exc} and N, respectively.

Given the rather low temperatures derived from the rotational diagrams, we infer that the CH$_3$CCH emission originates from a cooler gas in the outer envelope of the source, in accordance with other observational works toward star-forming regions (Churchwell & Hollis 1983; Nagy et al. 2015; Andron et al. 2018; Hervías-Caimapo et al. 2019). Thus, we expect CH$_3$CCH to trace a more extended region. The rotational diagram constructed for an extended source (size of 10″) is displayed in the bottom panel of Figure 2. From the fit under the optically thin assumption ($\chi^2_{red} = 1.42$), we derived $N(CH_3CCH) = (6.9 \pm 0.4) \times 10^{15}$ cm^{-2} and $T_{exc} = 52 \pm 1$ K.

After including the opacity correction factor, we derived $N(CH_3CCH) = (7.5 \pm 0.4) \times 10^{15}$ cm^{-2} and $T_{exc} = 50 \pm 1$ K from the fit ($\chi^2_{red} = 1.51$). These values were employed to model the emission of CH$_3$CCH under LTE conditions with WEEDS (see Figure 3). Overall, the synthetic spectra are in good agreement with the observations, although the accordance is sensibly higher for K-ladders with lower J quantum numbers (see the discussion in Section 4.2). For the 10″ source size, the contribution of C_τ to the diagram is much less significant than for more compact emissions. Indeed, the corrected fit yielded T_{exc} and N values only slightly different from the optically thin scenario, with respective changes of -2.09% and 8.69%. Table 2 summarizes the excitation temperatures and column densities derived from the rotational diagram analyses.

In terms of the reduced χ^2 values, the fit of the 5″ diagram with opacity corrections was less accurate in comparison with the uncorrected counterpart, whereas no significant change was observed for the 10″ diagrams. This is a consequence of the underestimation of the source size in the 5″ scenario, which is compensated by overestimating the lines' optical depth—in particular, for the $K = 0$ and $K = 1$ transitions at lower J values (see Figure 3). Indeed, the CH$_3$CCH emission seems to be optically thin (Churchwell & Hollis 1983; Fontani et al. 2002), especially for the range of J quantum numbers observed in this work.

---

[16] http://cassis.irap.omp.eu/docs/RadiativeTransfer.pdf
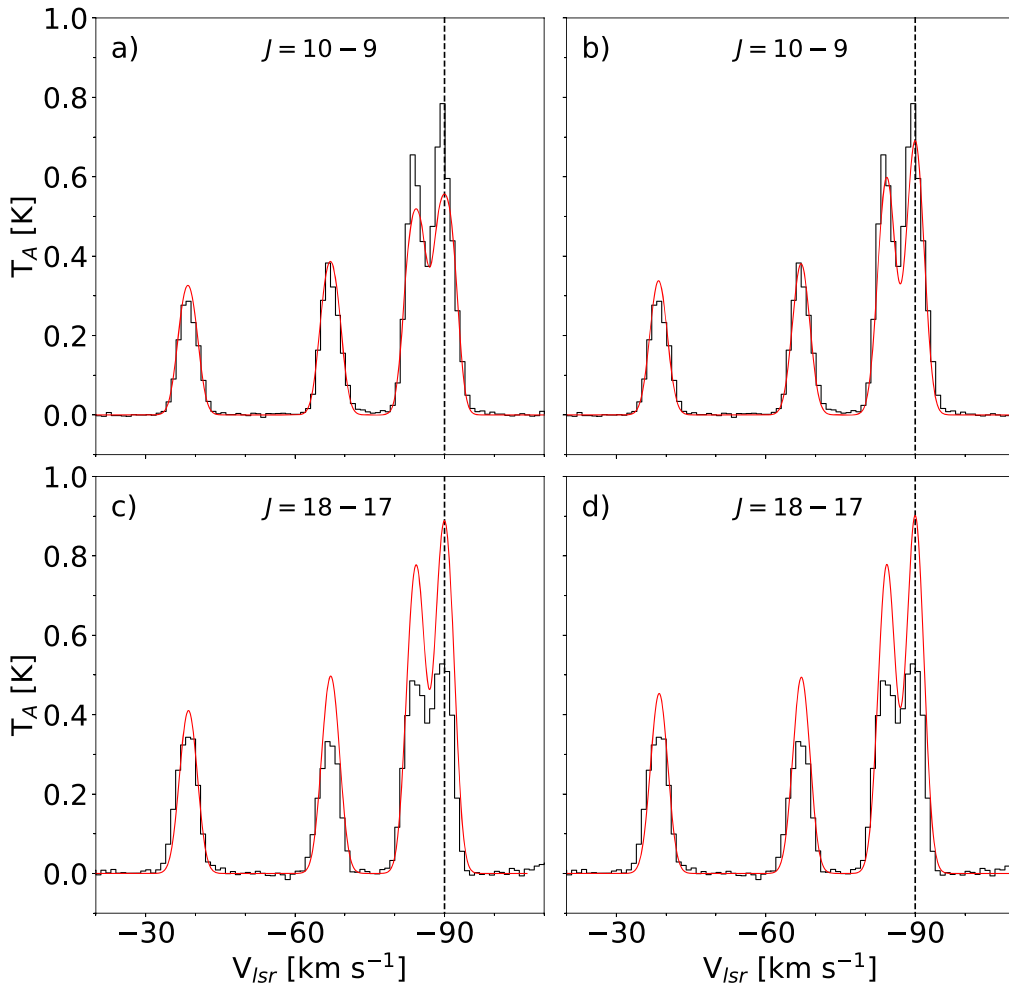
Figure 3. Spectra of CH_3CCH observed toward G331. Top panels: $J = 10–9$, $\sim$170.87–170.91 GHz; bottom panels: $J = 18–17$, $\sim$307.52–307.59 GHz. Left panels: LTE models simulated for a compact emission (5″); right panels: LTE models simulated for an extended emission (10″). For all panels, the black and red spectra correspond to the observations and the LTE models, respectively. The dashed line indicates the systemic velocity of the source. The abscissas of all spectra were adjusted to the systemic velocity of the $K = 0$ transition.

Table 2
Values of T_{exc} and N of CH_3CCH toward G331 Obtained from the Analysis of the Rotational Diagrams

Parameter	Source Size: 5″		Source Size: 10″	
	With C_τ	Without C_τ	With C_τ	Without C_τ
T_{exc} (K)	42 ± 1	51 ± 1	50 ± 1	52 ± 1
N ($\times 10^{16}$ cm^{-2})	4.5 ± 0.3	2.5 ± 0.1	0.75 ± 0.04	0.69 ± 0.04
χ^2_{red}	2.57	1.49	1.51	1.42

Table 3
Spectroscopic Parameters Employed in the Spectrum Simulations

Parameter	Value	Parameter	Value
A (MHz)	158,590 (a)	H_J (Hz)	0.0097 (b)
B (MHz)	8545.87712 (b)	H_{JK} (Hz)	0.935 (b)
D_J (kHz)	2.9423 (b)	H_{KJ} (Hz)	5.23 (b)
D_{JK} (kHz)	163.423 (b)	μ (D)	0.75 (c)

**References.** (a) JPL database; (b) Dubrulle et al. (1978); (c) Muenter & Laurie (1966).

3.3. Relative Intensities

The relative intensities of the lines within a K-ladder will change depending on the temperature of the environment. To explore this relation, the rotational spectra of CH_3CCH were simulated at temperatures ranging from 10 to 100 K, using the PGOPHER general purpose software (Western 2016). The rotational constants (A and B), the quartic and sextic centrifugal distortion constants (D_J, D_{JK}, H_J, H_{JK}, and H_{KJ}), and the dipole moment (μ) employed in the simulations are listed in Table 3.

The transition intensities are given by Western (2016):

$$I = \frac{S}{Q(T)}\left[\exp\left(\frac{-E_l}{k_B T}\right) - \exp\left(\frac{-E_u}{k_B T}\right)\right], \qquad (3)$$

which is simply the line strength S times the Boltzmann factor, normalized to the partition function $Q(T)$ at the given temperature. E_l and E_u correspond to the energies of the lower and upper states, respectively. In Figure 4, we plot the intensity ratios $I[K = n]/I[K = 0]$ of the predicted lines within a K-ladder
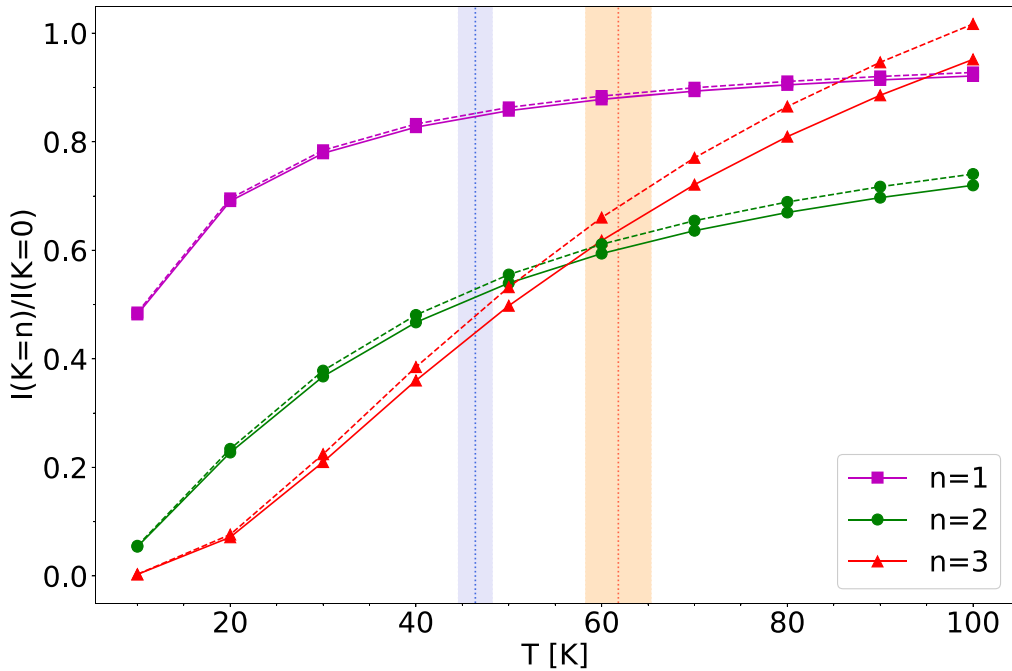
Figure 4. Intensity ratios $I[K=n]/I[K=0]$ vs. temperature for transitions within a given K-ladder. Purple squares represent ratios with $n=1$, green circles represent ratios with $n=2$, and red triangles represent ratios with $n=3$. The solid and dashed lines correspond to, respectively, the $J=10\text{--}9$ and $J=18\text{--}17$ K-ladders. The red and blue regions represent upper and lower limits to the temperature profile of the source and are discussed in Section 4.2.

versus the temperature, with $n=1$, 2, and 3. We show the results for the $J=10\text{--}9$ and $J=18\text{--}17$ transitions, corresponding to the extremes of the observed bandwidth.

As seen in the plot, the behaviors of the intensity ratios are overall analogous for the range of J values explored in this work. At low temperatures, the spectrum is dominated by the $K=0$ transitions, with small contributions from the other K levels. As the temperature rises, however, the ratios of all K transitions increase at different rates. The intensity ratios of both $K=1$ and $K=2$ transitions, compared to $K=0$, follow a similar trend. They show an initial stage of rapid growth, which becomes gradually slower as the temperature continues to rise. As can be seen for the $K=1$ transitions, the curve will eventually reach a plateau, which stabilizes the $K=1/K=0$ intensity ratios at values around 0.8–0.9. Comparatively, the ratios for $K=3$ present a more dramatic increase. At around 50 K, the $K=3$ lines become more intense than the $K=2$ transitions. Further, at around 100 K, their intensities surpass those of the $K=1$ transitions. At even higher temperatures, they ultimately become the most intense line of the given K-ladder.

This behavior can be explained by nuclear spin statistics: symmetric tops with three equivalent hydrogens, such as CH_3CCH, have two different spin symmetries—namely, A and E. The A states correlate with the transitions with $K=0$, 3, 6, 9, ..., whereas the E states correspond to the remaining transitions, such as $K=1$, 2, 4, 5, ... (e.g., Strom et al. 2020). Those states have relative statistical weights of A:E = 2:1 (Herzberg 1945), and therefore the population distribution of the transitions at higher temperatures will favor the $K=3$ states. At lower temperatures, however, the energy acts as a limiting factor. This phenomenon makes the CH_3CCH K-ladder profile highly sensitive to the local temperature, in

particular with regard to the relative intensities of the $K=3$ transitions.

As can be seen in Figure 1, we serendipitously observed a frequency window in which the CH_3CCH K-ladder profiles gradually change as a function of the rotational quantum number. For low J values, which are associated with cooler regions, the $K=2$ lines are more intense than the $K=3$ lines (see panel (a)). However, as we observe transitions with higher J values, which are consequently associated with warmer regions, the $K=2/K=3$ intensity ratios consistently decrease. From $J=15\text{--}14$ onward, the $K=3$ lines become more intense than the $K=2$ (see panel (i)). In Figure 5, we plot the $K=2/K=3$ ratios of the observed areas listed in Table 1 as a function of the upper J value. This plot yields a Pearson correlation coefficient of $r=-0.84$, which, given the small FWHM dispersion of the observed lines, clearly indicates a decreasing trend of the $K=2/K=3$ intensity ratios with J. This result strongly suggests that the lines are tracing a region with a temperature gradient, as will be discussed in Section 4.2.

3.4. Search for the CH_3CCH Isotopologues

The ^{13}C isotopologues of CH_3CCH, as well as its deuterated forms, have been successfully detected toward multiple interstellar sources (Gerin et al. 1992; Markwick et al. 2002, 2005; Belloche et al. 2013; Potapov et al. 2016; Halfen et al. 2017; Agúndez et al. 2019; Schmidt & Ziurys 2019). Recently, Agundez et al. (2021) have detected the two doubly deuterated forms of methyl acetylene—CHD_2CCH and CH_2DCCD—toward the dense core L483. They derived abundance ratios of $CH_3CCH/CHD_2CCH = 34 \pm 10$ and $CH_3CCH/CH_2DCCD = 42 \pm 13$, which are only a few times less than the singly deuterated counterparts.

Motivated by the copious amount of CH_3CCH line detections in G331, we searched across the survey for the ^{13}C
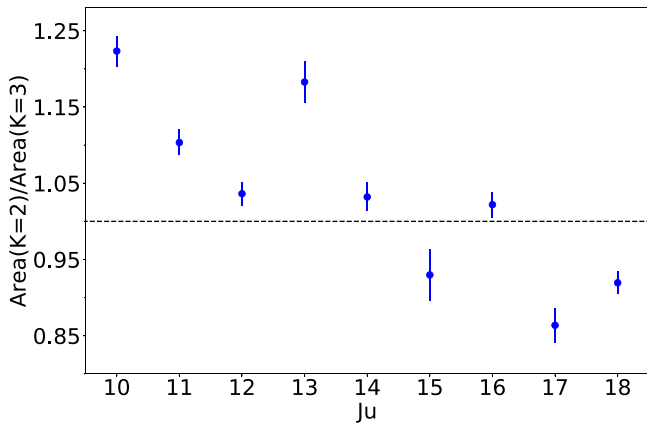
Figure 5. Ratios of the areas for $K = 2$ and $K = 3$ lines vs. the upper J value of the transition. Areas and uncertainties were obtained through Gaussian fittings of the observed data using CLASS. The dashed line indicates a ratio of unity.

Figure 6. Modeled $10_K–9_K$ K-ladder of $^{13}CH_3CCH$ (in red) superimposed on the spectrum observed toward G331 (in black).

and D isotopologues of CH_3CCH. Only the $10_0–9_0$ and $10_1–9_1$ lines of $^{13}CH_3CCH$ were detected above the 3σ threshold. However, they are blended, and just marginally above the detection limit, and so we cannot reliably confirm these detections. Assuming a ratio of $^{12}C/^{13}C \sim 20$, as estimated for G331 and other sources toward the Galactic center (Wilson & Rood 1994; Requena-Torres et al. 2006; Mendoza et al. 2018; Duronea et al. 2019; Yan et al. 2019), we derive a $^{13}CH_3CCH$ column density of $N \sim 3.75 \times 10^{14}$ cm^{-2}. This column density was used to model the emission of the $10_K–9_K$ K-ladder of $^{13}CH_3CCH$ under LTE conditions (Figure 6), which is shown to be consistent with the observed spectrum of G331.

4. Discussion

4.1. Origin of the Emission

Hervías-Caimapo et al. (2019) have observed several molecular lines toward G331 and classified them according to the line profile, with narrow lines tracing the emission from the core ambient medium and lines with broad wings tracing the outflow and shocked region. Accordingly, we expect from the narrow line profiles that the observed CH_3CCH emission originates from a quiescent (not expanding) core medium. This region is also associated with lower temperatures (below 100 K), which is consistent with the excitation temperatures derived from the rotational diagram. A schematic view of the physical model of G331, which considers the emission of CH_3CCH and other molecular tracers, is presented in Figure 7.

4.2. Physical Conditions: Gas Temperatures

In Section 3.4, we discussed the dependence of the $K = 2/K = 3$ intensity ratios of CH_3CCH with increasing temperatures. This inversion in relative populations within the same K-ladder is observed toward G331 and can be easily inferred by visual inspection (see Figure 1).

States with higher J quantum numbers require higher energies to be populated and therefore tend to be associated with warmer regions than the lower J states. Given that the $K = 2/K = 3$ intensity ratios are negatively correlated with J (see Figure 5), we suggest that the CH_3CCH emission is in fact described by a temperature gradient, which explains the behavior seen in Figure 1. In order to estimate the extent of
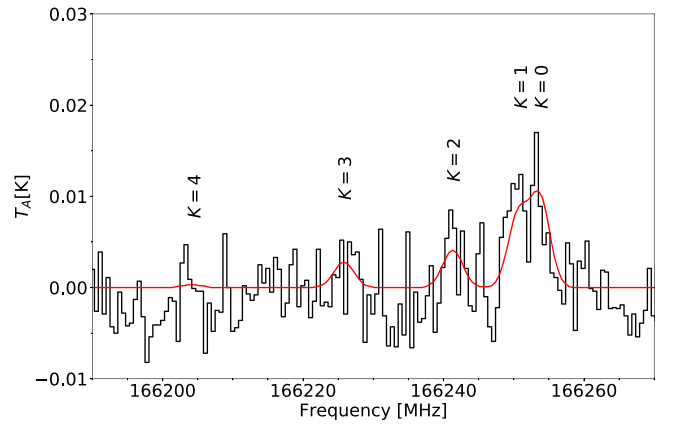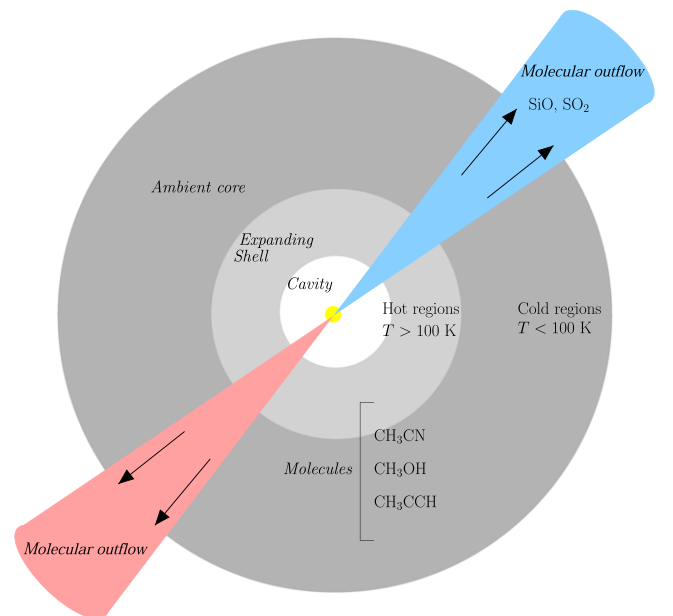

Figure 7. Schematic view of the physical model proposed for G331. Based on the models of Merello et al. (2013b), Duronea et al. (2019), and Hervías-Caimapo et al. (2019).

the temperature gradient, we have grouped the points in the rotational diagram into two subsets (Figure 8) separated at $E_{up} \approx 125$ K—according to the behavior of the $K = 2/K = 3$ intensity ratio of the K-ladder: the lower-energy group contains all $K = 2$ transitions with $J \leqslant 14$, for which $K = 2/K = 3 \gtrsim 1$. Contrarily, the higher-energy subset encompasses all $K = 2$ transitions with $J > 14$, for which $K = 2/K = 3 \lesssim 1$. The resulting T_{exc} and N obtained from the linear fit of each subset are listed in Table 4.

Assuming an optically thin scenario, the rotational diagram divided into two subsets yields temperature components of ~ 45 and ~ 60 K. Although the points in the rotational diagram show an overall fairly linear trend, the T_{exc} obtained from this analysis is highly sensitive to the fitted slope. Consequently, a difference of around 15 K arises between the derived values from the linear fittings of the two subsets. This temperature interval coincides with the region of Figure 4 where the
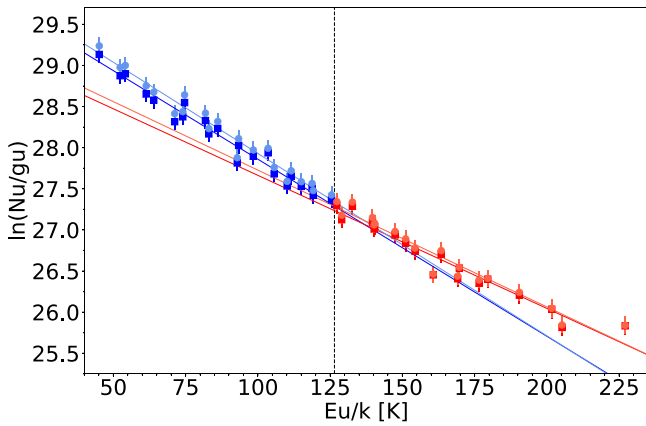
Figure 8. Rotational diagram of the CH$_3$CCH lines for a source size of 10″. The points were divided into two subsets indicated by the dashed line. The points pertaining to the low- and high-energy subsets are shown in blue and red, respectively. Least-squares fits to the points within each subset are shown. Circles and squares correspond to the lines with and without opacity corrections, respectively.

Table 4
Values of $T_{\rm exc}$ and N of CH$_3$CCH Obtained from the Two-component Rotational Diagrams for a Source Size of 10″

Parameter	Lower-energy Comp. (Blue)		Higher-energy Comp. (Red)	
	With C_τ	Without C_τ	With C_τ	Without C_τ
$T_{\rm exc}$ (K)	45 ± 2	46 ± 2	60 ± 3	62 ± 3
N ($\times 10^{15}$ cm^{-2})	7.9 ± 0.6	7.2 ± 0.5	5.7 ± 0.9	5.3 ± 0.8
$\chi^2_{\rm red}$	0.87	0.82	1.19	1.14

intensity inversion of $K = 2$ and $K = 3$ occurs. Thus, one can regard the two temperature components extracted from the blue and red subsets in Figure 8 as, respectively, lower and upper limits to the temperature profile of the observed emitting region —indicated as the blue and red regions in Figure 4. The rotational diagram analysis of Section 3.2 is therefore suited to evaluate the large-scale emission of CH$_3$CCH, yielding an average temperature of $T_{\rm exc} \sim 50.2$ K. The intrinsic spectroscopic properties of methyl acetylene, however, enabled us to perform a more direct and meticulous assessment of the temperature of the source. The same discussion is valid for the optically thick scenario.

The synthetic spectra under the LTE assumption shown in Figure 3 reproduce more accurately the observed data for lower J quantum numbers. This gradual loss in accuracy for higher J transitions is likely a consequence of the temperature profile that leads to the intensity inversion around $J_u = 14$ (see Figure 5). Indeed, throughout the entire $\sim$170,840–307,600 MHz frequency range, modeled transitions with $K = 3$ are less intense than the $K = 2$ counterparts. Since using only one temperature component is not completely adequate to describe our observations, the model will be increasingly amiss as the bulk of the emission transits to regions with different average gas temperatures. Hence, our LTE model seems to best describe the cooler environment, traced by the lines with lower J values.

Previously, Hervías-Caimapo et al. (2019) have used ALMA to observe four CH$_3$CCH lines within the $J = 21$–20 K-ladder toward G331, which showed a peak of emission located at a radius of $\sim$1″2. From the rotational diagram constructed with

the CH$_3$CCH lines, they obtained an excitation temperature of $T_{\rm exc} = 70 \pm 7$ K. Their results are in accordance with our hypothesis of a temperature gradient, which indeed predicts that transitions with higher J quantum numbers will be associated with higher excitation temperatures and more compact regions.

4.3. Kinematics

The spectroscopic parameters (see Table 1), obtained through fitting a Gaussian profile to each line, are directly related to the kinematics of the emitting region—or, at least, of the gas where the bulk of the emission originates. In Figure 9, we present a plot of the widths and peak velocities of the observed lines, which are listed in Table 1.

The line widths and peak velocities of transitions with the same quantum number K are overall strongly correlated. Indeed, the Pearson correlation coefficients of the $K = 0$, $K = 1$, $K = 2$, and $K = 3$ groups are, respectively, $r = -0.85$, $r = -0.97$, $r = -0.78$, and $r = -0.80$. This coefficient measures the linear correlation between two variants by means of the ratio of their covariance and the product of their standard deviation. Thus, $r = \pm 1$ corresponds to perfect linear correlations (either positive or negative), and $r = 0$ corresponds to no correlation. The lines with $K = 4$ are fainter and harder to observe and therefore were not included in the comparison. Their smaller signal-to-noise ratios hamper their analysis, which is reflected in their higher associated uncertainties reported in Table 1. Nonetheless, for each K group, there is a clear tendency for broader lines to present increasingly blueshifted velocities. The same trend was also observed by Di Francesco et al. (2004) for bright ($T_{\rm B}^{\rm max} \geqslant 10\sigma$) N$_2H^+$ lines toward the Ophiuchus A star-forming core: they found that the higher-velocity lines were systematically broader, which they associate with infalling motions that increase local rotation speeds.

Interestingly, the $K = 0$ lines are systematically broader and less blueshifted than the other groups, indicating that they might be tracing a slightly different region than the bulk of the emission of the other K transitions. At low temperatures, the contributions from transitions with $K \neq 0$ to the rotational spectrum of CH$_3$CCH are minor (see Figure 4), and the emission is dominated by the $K = 0$ lines. As the temperature rises, the relative intensities of the $K \neq 0$ transitions rapidly increase, resulting in richer K-ladders. Thus, it is likely that the bulk of the $K = 0$ emission originates from a cooler and more extended region, which does not contribute as significantly to the lines with $K \neq 0$. These, in turn, must be tracing a hotter and more compact environment, resulting in a different kinematic signature. The systematic redshift of the peak velocities for the $K = 0$ lines compared to the other groups also suggests interesting velocity features of the cold component. It is worth mentioning that the mean velocity shift between lines with the same quantum number K within the $J = 10$–9 and $J = 18$–17 K-ladders is $\sim$0.49 km s^{-1}, which is more than three times the poorest obtained velocity resolution. Further surveys of the CH$_3$CCH emission toward G331 with higher angular resolution are imperative to better understand the different gas components and the small-scale structure of the hot core.

In Figure 10, we show a comparison of the line widths versus the rest frequency, together with their Pearson coefficients. From the plots, it is clear that the FWHM is
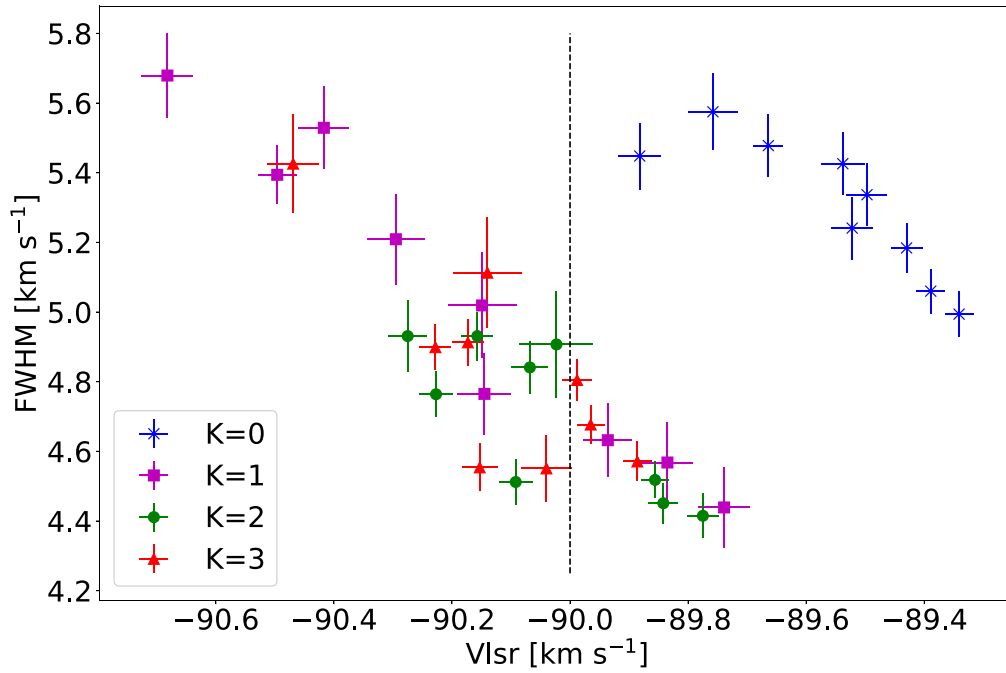
Figure 9. Line widths vs. peak velocities obtained from Gaussian fittings of the observed transitions. Blue crosses represent transitions with $K = 0$, purple squares represent transitions with $K = 1$, green circles represent transitions with $K = 2$, and red triangles represent transitions with $K = 3$. The black dashed line separates the blue- and redshifted regions relative to the adopted systemic velocity of G331 (-90 km s^{-1}).
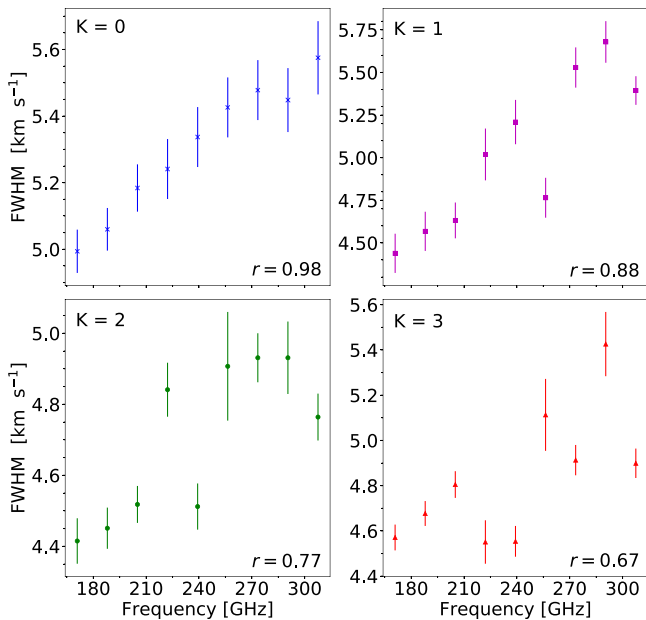
Figure 10. Line widths vs. rest frequencies obtained from Gaussian fittings of the observed transitions with $K = 0$, $K = 1$, $K = 2$, and $K = 3$.

Table 5
Abundances of CH$_3$CCH relative to H$_2$ and CH$_3$OH Observed toward High-mass Star-forming Sites

Source	$/N(\mathrm{H}_2)$	$/N(\mathrm{CH_3OH})$	$T_{\mathrm{exc}}^{\mathrm{CH_3CCH}}$
G12.89+0.49 (a)	$4.2^{+2.8}_{-2.2} \times 10^{-8}$	$0.34^{+0.28}_{-0.15}$	33^{+20}_{-9}
G16.862.16 (a)	$3.2^{+1.9}_{-1.5} \times 10^{-8}$	$0.36^{+0.28}_{-0.18}$	29^{+15}_{-8}
G28.280.36 (a)	$7.6^{+5.2}_{-4.4} \times 10^{-8}$	$1.61^{+1.4}_{-0.86}$	23^{+9}_{-6}
ATLASGAL (b)	$(0.5\text{--}2.5) \times 10^{-8}$ (b)	0.31^a	$34.5^{+24.6}_{-10.5}$
NGC 7538 IRS9 (c)	n.p.	1.3 ± 0.4	47 ± 5
W3 IRS5 (c)	n.p.	2.2 ± 0.7	58 ± 8
AFGL490 (c)	n.p.	1.8 ± 0.8	41 ± 7
G331 (this work)	$(0.8\text{--}2.8) \times 10^{-8}$	0.42 ± 0.05	50 ± 1

Notes. n.p. = not provided. The excitation temperatures are given in units of K.
[a] Derived from the average abundances reported by Giannetti et al. (2017).
References. (a) Taniguchi et al. (2018); (b) Giannetti et al. (2017); (c) Fayolle et al. (2015).

4.4. CH$_3$CCH Abundances

The abundance of CH$_3$CCH relative to H$_2$ ($X(\mathrm{CH_3CCH})$) is defined as the ratio of the column densities $N(\mathrm{CH_3CCH})/N(\mathrm{H_2})$. We have estimated the H$_2$ column density in G331 from ALMA measurements of $N(\mathrm{H^{13}CO^+}) \approx (1.5\text{--}3.2) \times 10^{13}$ cm^{-2} (Merello et al. 2013a, 2013b; Hervías-Caimapo et al. 2019), adopting an abundance ratio $N(\mathrm{H^{13}CO^+})/N(\mathrm{H_2}) = 3.3 \times 10^{-11}$, as measured by Blake et al. (1987) in Orion KL. Additionally, a hydrogen column density of $N(\mathrm{H_2}) = 2.7 \times 10^{23}$ cm^{-2} was reported for G331 from the continuum emission's surface density at 1.2 mm (Duronea et al. 2019). Considering those two limits for $N(\mathrm{H_2})$, we derived a ratio of $X(\mathrm{CH_3CCH}) \approx (0.8\text{--}2.8) \times 10^{-8}$.

In Table 5, we present a comparison of the CH$_3$CCH abundances with respect to H$_2$ in different massive-star-forming regions, including G331. Our derived abundance and excitation temperature agree well with the ones obtained for

correlated to the line frequency, particularly for the lines with $K = 0$ and $K = 1$. Since thermal broadening effects are negligible for radio transitions at the considered temperature range (see, e.g., the discussion of Fontani et al. 2002), the broader widths associated with higher J values indicate that the gas where the bulk of the emission originates must become gradually more turbulent as the temperature increases. This is fairly reasonable, considering that the warmer emission comes from the inner parts of the envelope surrounding the massive young stellar object (MYSO).

similar sources, which indicates similarities in the formation pathway of this molecule at such environments. The fact that this abundance comes mostly from the enveloping gas reinforces the conclusions drawn by other works (e.g., Öberg et al. 2013; Fayolle et al. 2015; Giannetti et al. 2017; Taniguchi et al. 2018) that the formation of methyl acetylene is not limited by heat input and should take place during the earlier stages of star formation. In other words, CH_3CCH is likely a so-called zeroth-generation molecule (Herbst & van Dishoeck 2009). Nonetheless, in the case of solid-phase formation, heat will eventually be required in order for the molecule to desorb to the gas phase.

We also estimate the fractional abundance of CH_3CCH with respect to methanol, $N(CH_3CCH)/N(CH_3OH)$, to be 0.42 ± 0.05. This value is listed in Table 5, together with the ratios obtained from the literature for other massive-star-forming regions. The methanol column density in G331 is assumed to be of $\approx (1.8 \pm 0.2) \times 10^{16}$ cm^{-2}, as derived by Mendoza et al. (2018) under the LTE formalism and assuming the total CH_3OH abundance as the sum of the A-CH_3OH and E-CH_3OH contributions. This methanol emission, however, is thought to originate from a region of only $5''3$, which is considerably more compact than the emitting region of CH_3CCH. Given that the envelope abundance of methanol in G331 is not fully known, the derived $N(CH_3CCH)/N(CH_3OH)$ ratio is likely artificially lower than in reality. Nonetheless, it is still fairly close to the ratios derived in other sources, further strengthening the conclusion that they present similar chemistry.

5. Chemical Modeling

Formation pathways of CH_3CCH in the interstellar medium include gas-phase ion-neutral routes with $C_2H_2^+$ as a precursor (Schiff & Bohme 1979; Millar & Freeman 1984), neutral–neutral reactions such as $CH + C_2H_4 \rightarrow CH_3CCH + H$ (Turner et al. 1999), and dissociative recombination reactions involving larger hydrocarbons (Calcutt et al. 2019). Grain-surface reactions are also proposed in order to explain the observed abundances of CH_3CCH (Hickson et al. 2016; Guzmán et al. 2018). Regarding massive environments, Taniguchi et al. (2019) have constructed hot-core models to investigate the formation pathways of cyanopolyynes and other carbon-chain species, including CH_3CCH and c-C_3H_2, around MYSOs. They found chemical similarities between methyl acetylene, methane, and cyanopolyynes, all being triggered by CH_4 sublimation from dust grains. Furthermore, those species are also shown to accumulate in the bulk of the ice until the temperature reaches their respective sublimation points. Comparatively, small reactive hydrocarbons such as CCH and CCS are shown not to accumulate onto dust grains, being readily destroyed in the gas phase instead. Complementarily, Andron et al. (2018) discuss the formation routes of methyl acetylene in the solar-type protostar IRAS 16293–2422. They show that, at large distances from the central star, the abundance of CH_3CCH in the solid phase is higher than in the gas phase, which indicates that it is efficiently produced on dust grains at low temperatures through successive hydrogenation of C_3. Moreover, their models also indicate that reactions in the gas phase with C_2H_4 and C_3H_5 as precursors can also effectively form methyl acetylene in the outer envelope.

In order to investigate the chemical evolution of CH_3CCH in G331, we constructed a time-dependent chemical model of the

Table 6
Initial Gas-phase Elemental Abundances, with the Format $a(b)$ Representing $a \times 10^b$

Element	n_i/n_H^a	Ref.	Element	n_i/n_H^a	Ref.
H_2	0.5		He	9.0(−2)	1
N	6.2(−5)	2	O	2.4(−4)	3
C^+	1.7(−4)	2	S^+	1.5(−5)	2
Fe^+	3.0(−9)	4	Si^+	8.0(−9)	4
Na^+	2.0(−9)	4	Mg^+	7.0(−9)	4
Cl^+	1.0(−9)	4	P^+	2.0(−10)	4
F	6.7(−9)	5			

References. (1) Wakelam & Herbst (2008); (2) Jenkins (2009); (3) Hincelin et al. (2011); (4) low-metal abundances from Graedel et al. (1982); (5) depleted value from Neufeld et al. (2005).

source using the three-phase gas-grain Nautilus code (Ruaud et al. 2016), in which the grain-surface chemistry is distinguished from the bulk of the ice. The model consists of two zero-dimensional steps (i.e., the physical properties of the source are uniform and static), comprising the dark-cloud and the hot-core phases of star formation. The first step, representing an initial dark-cloud phase, was computed using the elemental abundances listed in Table 6, as was computed in previous works about the chemistry of HNCO in G331 (Canelo et al. 2021). For the physical parameters, we adopted a gas temperature and density of 10 K and 1×10^4 cm^{-3}, respectively. Then, we employed the abundances derived from the dark-cloud model after 10^5 yr as initial parameters for the second step: a "rapid" hot-core phase. For this second period we used $T = 80$ K and tested four different values for n_{H_2}: 1×10^6 cm^{-3}, 5×10^6 cm^{-3}, 1×10^7 cm^{-3}, and 5×10^7 cm^{-3}. The gas and dust temperatures were set as equal throughout the entire simulation, as they have been shown to be coupled in dense sources (Merello et al. 2019). Moreover, standard visual extinction ($A_V = 10$ mag) and cosmic-ray ionization rates ($\zeta = 1.3 \times 10^{-17}$ cm^{-3}) were used. The standard chemical network presented in the KInetic Database for Astrochemistry (KIDA;[17] Wakelam et al. 2015) catalog was employed in the simulations.

The temporal evolution of the CH_3CCH abundance derived from the hot-core model for the different hydrogen densities is presented in Figure 11. The abundance derived from our observations is best predicted by the model with $n_{H_2} = 5 \times 10^6$ at timescales as early as $\sim 10^3$ yr, in agreement with the expected age of this source (Merello et al. 2013a). This is consistent with an extended and thus less dense emitting gas, as was inferred from the radiative analyses. Furthermore, the steady-state plateau in abundance reached after $\sim 10^3$ yr is consistent with the hypothesis of CH_3CCH accumulating onto dust grains and enriching the gas phase upon desorption. Experiments on interstellar ice analogs exposed to energetic electrons resulted in the formation of CH_3CCH, among other related molecules (Abplanalp et al. 2019), which supports this hypothesis. Complementary observations of different species with related chemical networks are desirable to build a comprehensive view on the properties of the source and will be included in future works focused on constructing a thorough chemical and physical model of G331.

---

[17] http://kida.obs.u-bordeaux1.fr/
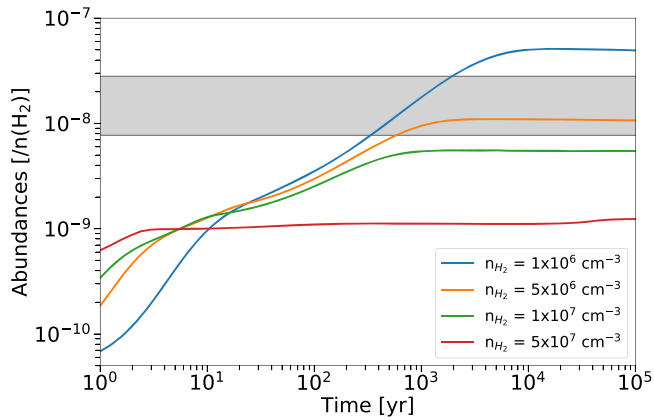
Figure 11. Abundance of CH₃CCH as a function of time, obtained from the hot-core model for different initial densities of H₂. The gray area indicates the methyl acetylene abundance derived from the observations.

6. Conclusions

We have conducted a spectral survey of CH₃CCH toward the HMC G331.512-0.103, resulting in the detection of 41 lines without contamination. To the best of our knowledge, this was the first spectral survey of methyl acetylene toward the source, resulting in interesting insights on the physics of the source. The spectral analysis was performed through rotational diagrams, assuming LTE, from which we derived an averaged excitation temperature of ∼50 K for an extended emission. Thus, the bulk of the CH₃CCH emission likely originates from a warm and extended gas, associated with the ambient core region of G331. Moreover, we obtained $N(CH_3CCH) = 7.5 \times 10^{15} cm^2$, $X[CH_3CCH/H_2] \approx (0.8–2.8) \times 10^8$, and $X[CH_3CCH/CH_3OH] \approx 0.42 \pm 0.05$ from the observations, which are consistent with other single-dish observational works toward massive-star-forming regions and suggest that CH₃CCH is a zeroth-generation molecule with similar chemistry throughout these environments.

The $K = 2/K = 3$ line-intensity ratios of transitions within a given K-ladder are strongly negatively correlated with J_u, which firmly suggests that the emission is arising from a region with a temperature gradient. An analysis of the rotational diagram separated into two subsections provides upper and lower limits of, respectively, ∼60 and ∼45 K for the temperature gradient. This approach enables us to assess the small-scale structure of the source with data from single-dish facilities. For a thorough analysis of the temperature profile, however, it is imperative to observe a wide range of CH₃CCH lines with a high angular resolution, by means of interferometry instruments such as ALMA.

The line widths of transitions with the same K quantum number are strongly correlated to their rest frequencies and peak velocities. Thus, we infer that the warmer regions, traced by the higher-frequency lines, are also associated with higher turbulence effects. Moreover, the $K = 0$ transitions seem to be tracing a slightly different region than the rest of the CH₃CCH lines, as indicated by its different kinematic signature. Surveys of this species with higher angular resolution are also fundamental to further explore the origin of this differentiation.

A chemical model of CH₃CCH in G331, comprising a dark-cloud phase followed by a hot-core collapse, predicts CH₃CCH abundances that agree with our observations for timescales of

$t \gtrsim 10^3$ yr and densities of $n_{H_2} \sim 5 \times 10^6 cm^{-3}$. This is in line with the expected age and size of this source.

ORCID iDs

Julia C. Santos ⬤ https://orcid.org/0000-0002-3401-5660
Leonardo Bronfman ⬤ https://orcid.org/0000-0002-9574-8454
Edgar Mendoza ⬤ https://orcid.org/0000-0001-9381-7826
Jacques R. D. Lépine ⬤ https://orcid.org/0000-0002-8969-0313
Manuel Merello ⬤ https://orcid.org/0000-0003-0709-708X

References

Abplanalp, M. J., Góbi, S., & Kaiser, R. I. 2019, PCCP, 21, 5378
Agúndez, M., Marcelino, N., Cernicharo, J., Roueff, E., & Tafalla, M. 2019, A&A, 625, A147
Agundez, M., Roueff, E., Cabezas, C., Cernicharo, J., & Marcelino, N. 2021, A&A, 649, A171
Allen, V., van der Tak, F. F. S., & Walsh, C. 2018, A&A, 616, A67
Andron, I., Gratier, P., Majumdar, L., et al. 2018, MNRAS, 481, 5651
Belitsky, V., Lapkin, I., Fredrixon, M., et al. 2018, A&A, 612, A23
Belloche, A., Garrod, R. T., Müller, H. S. P., & Menten, K. M. 2014, Sci, 345, 1584
Belloche, A., Garrod, R. T., Müller, H. S. P., et al. 2019, A&A, 628, A10
Belloche, A., Müller, H. S. P., Menten, K. M., Schilke, P., & Comito, C. 2013, A&A, 559, A47
Bergin, E. A., Goldsmith, P. F., Snell, R. L., & Ungerechts, H. 1994, ApJ, 431, 674
Bisschop, S. E., Jørgensen, J. K., van Dishoeck, E. F., & de Wachter, E. B. M. 2007, A&A, 465, 913
Blake, G. A., Sutton, E. C., Masson, C. R., & Phillips, T. G. 1987, ApJ, 315, 621
Bøgelund, E. G., Barr, A. G., Taquet, V., et al. 2019, A&A, 628, A2
Bonfand, M., Belloche, A., Garrod, R. T., et al. 2019, A&A, 628, A27
Bronfman, L., Casassus, S., May, J., & Nyman, L. Å. 2000, A&A, 358, 521
Bronfman, L., Cohen, R. S., Thaddeus, P., & Alvarez, H. 1985, in The Milky Way Galaxy, ed. R. van Woerden, J. Allen, & W. B. Burton, Vol. 106 (Dordrecht: Reidel)
Bronfman, L., Garay, G., Merello, M., et al. 2008, ApJ, 672, 391
Buhl, D., & Snyder, L. E. 1973, in Molecules in the Galactic Environment, ed. M. A. Gordon & L. E. Snyder (New York: Wiley), 187
Calcutt, H., Willis, E. R., Jørgensen, J. K., et al. 2019, A&A, 631, A137
Canelo, C. M., Bronfman, L., Mendoza, E., et al. 2021, MNRAS, 504, 4428
Caselli, P., Hasegawa, T. I., & Herbst, E. 1993, ApJ, 408, 548

Cazzoli, G., Lattanzi, V., Kirsch, T., et al. 2016, A&A, 591, A126
Cernicharo, J., McCarthy, M. C., Gottlieb, C. A., et al. 2015, ApJL, 806, L3
Cerqueira, H. B. A., Santos, J. C., Fantuzzi, F., et al. 2020, JPCA, 124, 6845
Cesaroni, R. 2005, in Massive Star Birth: A Crossroads of Astrophysics, ed.
    R. Cesaroni et al., Vol. 227 (Cambridge: Cambridge Univ. Press), 59
Cesaroni, R., Hofner, P., Walmsley, C. M., & Churchwell, E. 1998, A&A,
    331, 709
Churchwell, E., & Hollis, J. M. 1983, ApJ, 272, 591
Comito, C., Schilke, P., Phillips, T. G., et al. 2005, ApJS, 156, 127
Coutens, A., Jørgensen, J. K., van der Wiel, M. H. D., et al. 2016, A&A,
    590, L6
Di Francesco, J., André, P., & Myers, P. C. 2004, ApJ, 617, 425
Domenicano, A., & Hargittai, I. 1992, Accurate Molecular Structures: Their
    Determination and Importance (Oxford: Oxford Univ. Press)
Dubrulle, A., Boucher, D., Burie, J., & Demaison, J. 1978, JMoSp, 72, 158
Dumke, M., & Mac-Auliffe, F. 2010, Proc. SPIE, 7737, 77371J
Duronea, N. U., Bronfman, L., Mendoza, E., et al. 2019, MNRAS, 489, 1519
Endres, C. P., Schlemmer, S., Schilke, P., Stutzki, J., & Müller, H. S. P. 2016,
    JMoSp, 327, 95
Fayolle, E. C., Öberg, K. I., Garrod, R. T., van Dishoeck, E. F., &
    Bisschop, S. E. 2015, A&A, 576, A45
Fontani, F., Cesaroni, R., Caselli, P., & Olmi, L. 2002, A&A, 389, 603
Garay, G., & Lizano, S. 1999, PASP, 111, 1049
García, P., Bronfman, L., Nyman, L. Å., Dame, T. M., & Luna, A. 2014, ApJS,
    212, 2
Gerin, M., Combes, F., Wlodarczak, G., Encrenaz, P., & Laurent, C. 1992,
    A&A, 253, L29
Giannetti, A., Leurini, S., Wyrowski, F., et al. 2017, A&A, 603, A33
Gieser, C., Beuther, H., Semenov, D., et al. 2021, A&A, 648, A66
Gildas Team 2013, GILDAS: Grenoble Image and Line Data Analysis
    Software, Astrophysics Source Code Library, ascl:1305.010
Goldsmith, P. F., & Langer, W. D. 1999, ApJ, 517, 209
Gomez, Y., Garay, G., & Lizano, S. 1995, ApJ, 453, 727
Graedel, T. E., Langer, W. D., & Frerking, M. A. 1982, ApJS, 48, 321
Grubbs, G., & Cooke, S. 2010, JMoSp, 259, 120
Güsten, R., Nyman, L. Å., Schilke, P., et al. 2006, A&A, 454, L13
Guzmán, A. E., Guzmán, V. V., Garay, G., Bronfman, L., & Hechenleitner, F.
    2018, ApJS, 236, 45
Halfen, D. T., Woolf, N. J., & Ziurys, L. M. 2017, ApJ, 845, 158
Heaton, B. D., Little, L. T., & Bishop, I. S. 1989, A&A, 213, 148
Herbst, E., & van Dishoeck, E. F. 2009, ARA&A, 47, 427
Hervías-Caimapo, C., Merello, M., Bronfman, L., et al. 2019, ApJ, 872, 200
Herzberg, G. 1945, Molecular Spectra And Molecular Structure, Vol. II
    (New York: D. Van Nostrand Company, Inc.)
Hickson, K. M., Wakelam, V., & Loison, J.-C. 2016, MolAs, 3, 1
Hincelin, U., Wakelam, V., Hersant, F., et al. 2011, A&A, 530, A61
Hollis, J. M., Snyder, L. E., Blake, D. H., et al. 1981, ApJ, 251, 541
Jenkins, E. B. 2009, ApJ, 700, 1299
Jørgensen, J. K., Belloche, A., & Garrod, R. T. 2020, ARA&A, 58, 727
Krumholz, M. R. 2015, in in Very Massive Stars in the Local Universe, ed.
    J. S. Vink, Vol. 412 (Berlin: Springer), 43
Kuiper, T. B. H., Kuiper, E. N. R., Dickinson, D. F., Turner, B. E., &
    Zuckerman, B. 1984, ApJ, 276, 211
Lovas, F. J. 2004, JPCRD, 33, 177
Lovas, F. J., Johnson, D. R., Buhl, D., & Snyder, L. E. 1976, ApJ, 209, 770
Markwick, A. J., Charnley, S. B., Butner, H. M., & Millar, T. J. 2005, ApJL,
    627, L117
Markwick, A. J., Millar, T. J., & Charnley, S. B. 2002, A&A, 381, 560
Mauersberger, R., Henkel, C., Walmsley, C. M., Sage, L. J., & Wiklind, T.
    1991, A&A, 247, 307

McGuire, B. A. 2018, ApJS, 239, 17
McGuire, B. A., Martin-Drumel, M.-A., Thorwirth, S., et al. 2016, PCCP, 18,
    22693
Melli, A., Melosso, M., Tasinato, N., et al. 2018, ApJ, 855, 123
Mendoza, E., Bronfman, L., Duronea, N. U., et al. 2018, ApJ, 853, 152
Merello, M., Bronfman, L., Garay, G., et al. 2013a, ApJL, 774, L7
Merello, M., Bronfman, L., Garay, G., et al. 2013b, ApJ, 774, 38
Merello, M., Molinari, S., Rygl, K. L. J., et al. 2019, MNRAS, 483
    5355
Millar, T. J., & Freeman, A. 1984, MNRAS, 207, 405
Molinari, S., Merello, M., Elia, D., et al. 2016, ApJL, 826, L8
Muenter, J. S., & Laurie, V. W. 1966, JChPh, 45, 855
Müller, H. S. P., Schlöder, F., Stutzki, J., & Winnewisser, G. 2005, JMoSt,
    742, 215
Müller, H. S. P., Thorwirth, S., Bizzocchi, L., & Winnewisser, G. 2000,
    ZNatA, 55, 491
Müller, H. S. P., Thorwirth, S., Roth, D. A., & Winnewisser, G. 2001, A&A,
    370, L49
Nagy, Z., van der Tak, F. F. S., Fuller, G. A., & Plume, R. 2015, A&A,
    577, A127
Neufeld, D. A., Wolfire, M. G., & Schilke, P. 2005, ApJ, 628, 260
Öberg, K. I., Boamah, M. D., Fayolle, E. C., et al. 2013, ApJ, 771, 95
Pety, J., Teyssier, D., Fossé, D., et al. 2005, A&A, 435, 885
Pickett, H. M., Poynter, R. L., Cohen, E. A., et al. 1998, JQSRT, 60, 883
Potapov, A., Sánchez-Monge, Á., chilke, P., et al. 2016, A&A,
    594, A117
Puzzarini, C., Cazzoli, G., & Gauss, J. 2012a, JChPh, 137, 154311
Puzzarini, C., Cazzoli, G., López, J. C., et al. 2012b, JChPh, 137
    024310
Qiu, J., Zhang, J., Zhang, Y., Jia, L., & Tang, X. 2020, A&A, 634, A125
Requena-Torres, M. A., Martín-Pintado, J., Rodríguez-Franco, A., et al. 2006,
    A&A, 455, 971
Rosen, A. L., Offner, S. S. R., Sadavoy, S. I., et al. 2020, SSRv, 216, 62
Ruaud, M., Wakelam, V., & Hersant, F. 2016, MNRAS, 459, 3756
Santos, J. C. 2021, Master's thesis, University of Sao Paulo
Santos, J. C., Rocha, A. B., & Oliveira, R. R. 2020, JMoMo, 26, 278
Schiff, H. I., & Bohme, D. K. 1979, ApJ, 232, 740
Schmidt, D. R., & Ziurys, L. M. 2019, ApJL, 881, L38
Silva, A., Zhang, Q., Sanhueza, P., et al. 2017, ApJ, 847, 87
Snyder, L. E., Lovas, F. J., Hollis, J. M., et al. 2005, ApJ, 619, 914
Strom, A. I., Gutiérrez-Quintanilla, A., Chevalier, M., et al. 2020, JPCA,
    124, 4471
Tan, J. C., Beltrán, M. T., Caselli, P., et al. 2014, in Protostars and Planets VI,
    ed. H. Beuther et al. (Tucson, AZ: Univ. of Arizona Press), 149
Taniguchi, K., Herbst, E., Caselli, P., et al. 2019, ApJ, 881, 57
Taniguchi, K., Saito, M., Majumdar, L., et al. 2018, ApJ, 866, 150
Townes, C. H., & Schawlow, A. L. 1975, Microwave Spectroscopy (New
    York: Dover)
Turner, B. E., Terzieva, R., & Herbst, E. 1999, ApJ, 518, 699
Vassilev, V., Meledin, D., Lapkin, I., et al. 2008, A&A, 490, 1157
Vastel, C., Bottinelli, S., Caux, E., Glorian, J. M., & Boiziot, M. 2015, in
    SF2A-2015: Proc. Annual Meeting of the French Society of Astronomy and
    Astrophysics, ed. F. Martins et al. (Paris: SAF), 313
Wakelam, V., & Herbst, E. 2008, ApJ, 680, 371
Wakelam, V., Loison, J. C., Herbst, E., et al. 2015, ApJS, 217, 20
Western, C. M. 2016, JQSRT, 186, 221
Wilson, T. L., & Rood, R. 1994, ARA&A, 32, 191
Winnewisser, G., Lewen, F., Thorwirth, S., et al. 2003, CEJ, 9, 5501
Yan, Y. T., Zhang, J. S., Henkel, C., et al. 2019, ApJ, 877, 154
Zinnecker, H., & Yorke, H. W. 2007, ARA&A, 45, 481